

Manuscript version: Author's Accepted Manuscript

The version presented in WRAP is the author's accepted manuscript and may differ from the published version or Version of Record.

Persistent WRAP URL:

<http://wrap.warwick.ac.uk/161909>

How to cite:

Please refer to published version for the most recent bibliographic citation information. If a published version is known of, the repository item page linked to above, will contain details on accessing it.

Copyright and reuse:

The Warwick Research Archive Portal (WRAP) makes this work by researchers of the University of Warwick available open access under the following conditions.

© 2022 Elsevier. Licensed under the Creative Commons Attribution-NonCommercial-NoDerivatives 4.0 International <http://creativecommons.org/licenses/by-nc-nd/4.0/>.



Publisher's statement:

Please refer to the repository item page, publisher's statement section, for further information.

For more information, please contact the WRAP Team at: wrap@warwick.ac.uk.

Computational analysis of the mechanisms and characteristics for pulsating and uniform flame spread over liquid fuel at subflash temperatures

Baopeng Xu, Jennifer X Wen¹

Warwick Fire, School of Engineering, University of Warwick, Coventry, UK

Abstract

The present study aims to gain insight of the mechanisms and characteristics for pulsating and uniform flame spread over liquid fuel at subflash temperatures. A specific goal is to use the validated three-dimensional (3-D) numerical model to reveal fine details of the gas and liquid phase flows as well as the resulting flame characteristics, which are challenging to obtain experimentally. To facilitate the study, 3-D formulations have been developed to explicitly solve the transport equations in both phases. A compressible solver was formulated for flame propagation in the gas phase using a one-step chemical reaction expression and mixture-averaged diffusion coefficients for the gaseous species. An incompressible solver with temperature dependent thermo-physical properties was employed to describe the convective motions and heat transfer in the liquid fuel region. Validation has been conducted for both uniform and pulsating spreads over a narrow 1-propanol tray with varying fuel depths through comparing the predicted flame front evolution with published measurements. Further qualitative comparison has also been conducted for some predicted fine features of the gas and liquid phase flows and flame spreading characteristics with published experimental observations. For both the uniform and pulsating spread, the detailed flame structure including the main diffusion flame and a small stratified premixed flame at the front have been captured. Wherever relevant, the detailed predictions were also used to shed light on some discrepancies in previously reported features in different laboratory studies and numerical simulations. Finally, the detailed 3-D predictions were used to illustrate fine features of the subsurface convective flow and its relative position to the flame front, the relative magnitudes of the subsurface flow velocity and that of the spread rate as well as the role of the thermocapillary-driven subsurface flow in the flame spread mechanism.

Keywords

Pulsating and uniform flame spread; thermocapillary flow; subflash temperature; buoyancy effects

¹ Corresponding email Jennifer.wen@warwick.ac.uk

1. Introduction

Flame spread over liquid fuel is a classic combustion problem related to fire safety of fuel spills. The spreading characteristics is dependent on the flash point of the liquid fuel. If the initial fuel temperature is above the flash point, a flammable mixture of fuel vapor and air exists over the fuel surface and a steady flame spread will proceed through the combustible mixture readily formed through fuel evaporation. However, if the initial fuel temperature is below the flash point, the vapor concentration over the fuel surface is generally lower than the lean flammability limit (LFL) and the fuel needs to be preheated in order to evaporate and form a flammable mixture ahead of the flame front to facilitate the flame spread.

Akita [1] analysed the distinct spreading characteristics of flame over liquid fuels and identified three regimes in a decreasing order of the fuel temperature relative to its flash point, i.e. uniform, pulsating and pseudo-uniform. In both the uniform and pseudo-uniform regimes, the flame spreads in a steady/pseudo-steady rate. While in the pulsating regime, the flame displays a distinct pulsating behaviour with the flame front propagating in a regularly accelerating (jump stage) and decelerating (crawling stage) manner. The pseudo-uniform spread can also be regarded as pulsating but with an infinite wavelength. These spreading characteristics are controlled by flame-induced flows in both the gas and liquid fuel regions.

The flame heat feedback to the fuel surface is non-uniform especially beneath the flame front, thus inducing significant surface temperature gradients. Since the surface tension inversely varies with temperature, the surface temperature gradients produce thermocapillary (or Marangoni) convective motions [2] directed towards lower temperature regions. The thermocapillary effect coupled with the influences of both viscous and buoyant forces creates large scale convective motions inside the fuel region, significantly enhancing the heat transfer process [3]. The surface flow alters the gas flow conditions over the surface via the no-slip condition. The coupled flow conditions at the proximity of the flame front greatly affect the heat and mass transfer which are vital to flame spread at subflash temperatures.

A prerequisite condition for a flame to spread forward is the existence of a premixed combustible mixture ahead of the flame front above a quenching distance. Most previous studies [4-21] focused on the mass and heat transfer mechanism controlling the formation of the flammable mixture by investigating the flow dynamics and the distributions of temperature and species concentration around the flame front. Pulsating spread was observed as a main trailing diffusion flame with a pulsating flame front anchoring in a premixed region above the fuel surface. The propagating speed of the flame front is slower than the surface convective front during the crawling stage. The fuel surface temperature ahead of the flame front is elevated due to convective and radiative heat transfer. But as suggested by Akita [1], the subsurface flow is the dominant mechanism for the pulsating characteristics. A gas phase circulation cell was also observed ahead of the flame front [12], induced by the combined effects of the subsurface flow and the gas phase buoyancy. The circulation

cell facilitates the accumulation and mixing of fuel vapor. It was considered as the controlling mechanism for flame pulsation by Sirignano and Schiller [22]. The surface temperature was found not to decrease monotonically away from the flame front. Instead, a surface temperature valley just ahead of the flame front was observed by Glassman and Dryer [8] as well as Konishi et al. [21]. The temperature inside the surface valley is below the flash point, prohibiting the flame spread in the crawling stage and responsible for the pulsating mechanism [21]. The cold temperature valley was believed to be caused by the interaction of the subsurface flow and the buoyancy-induced liquid flow due to insufficient heating from the flame to a relatively cold liquid [21].

Akika [1] initially observed that there was no appreciable subsurface flow ahead of the flame front in the uniform regime. The liquid convective heat transfer was irrelevant to the fuel preheating and different preheating mechanisms have been proposed. He attributed the radiative and conductive heat transfer of gas phase to be the dominant mechanism. Glassman and Dryer [8] thought that the effect of radiative heat transfer was trivial in their small-scale laboratory tests and the gas conductive heat transfer was the only possible preheating mechanism. Hirano et al. [12] observed gas phase convective flow just ahead of the flame front and suggested that gas phase convective heat transfer and liquid phase conduction dominated the preheating mechanism. Ito et al. [13] observed a small region of subsurface flow just ahead of the flame front and suggested that liquid phase convection played an important role in the preheating. The gradual progression of the insight, although exerting differences in the underlying physical mechanisms, can be attributed to the level of details obtainable as confined by the experimental techniques used.

Despite the extensive studies, there still exist some important knowledge gaps on the flame spread mechanism over liquid fuel at subflash temperatures. Flame spread is a closely coupled problem of mass, momentum, and energy transfer between the gas and liquid phases. The flame front was observed to be located approximately 1mm above the fuel surface for alcohol fuels [21, 22]. The distributions of velocity, temperature and species concentration around the flame front are vital to gain further insight of the spreading mechanism, but it is still challenging for the current experimental techniques to obtain simultaneous three-dimensional (3-D) distributions of these parameters. Numerical modelling is potentially a powerful tool to obtain such insight.

Relatively fewer studies have been reported on numerical modelling of flame spread over liquid fuels [22, 26-30] in comparison with the relatively large number of experimental studies in the literature [1, 4-21, 23-25]. Di Blasi et al. [26] firstly proposed a coupled two-dimensional (2-D) model using constant fuel properties and one-step chemical kinetics to predict the pulsating spread and captured the experimentally observed features. Their study indicated that the surface convective flow was the dominant controlling factor. Schiller et al. [22] also proposed a coupled 2-D model, using temperature-dependent fuel properties, a single gas phase diffusion coefficient, one-step chemical kinetics and adaptive mesh, to predict both the

pulsating and uniform spreads. Their study revealed that the onset of pulsating spread was related to the formation of the gas phase recirculation cell but not the surface convective flow. They also found that the flame front exhibited features of both diffusive and lean premixed combustion during both pulsating and uniform spreads. The exact reasons for the inconsistency in their findings are difficult to assess, but the existence of such differences further emphasizes the need for physics-based modelling incorporating 3-D geometric arrangement and different fuel temperatures.

Although 2-D models can produce some useful qualitative results, previous experiments have proved that flame spread even at test scales is 3-D in nature and the effects of both the sidewalls and side air entrainment should be considered. Cai et al. [27-28] extended Schiller's 2-D model to 3-D by incorporating different species diffusion coefficients. The 3-D model captured a curved flame front resulting from the sidewall effects. This model was subsequently used to simulate the flame spread under opposed force flow conditions by Kim et al. [29].

Despite the useful insight provided by the above modelling efforts, there still exist considerable discrepancies between previous predictions and experimental observations. For example, the predicted recirculation zones in both the liquid and gas phases are smaller than that observed in the experiments [21]. Furthermore, the predictions for flame spread under quiescent microgravity conditions were also inconsistent with the experimental observation, e.g. a uniform spread was experimentally observed but a pulsating spread was predicted in [22]. By artificially amending the mass diffusivity and including a heat loss parameter, Miller et al. [30] successfully captured the differences in the flame spread characteristics under normal and microgravity conditions. Some previous 3-D numerical studies have also considered 3-D parameter distributions in the middle plane [27-29], but the effect of the sidewalls were not addressed.

In the present study, fully coupled 3-D numerical formulations have been developed to explicitly solve the transport equations in both the gas and liquid phases. A compressible solver was formulated for flame propagation in the gas phase while an incompressible solver with varied thermo-physical properties was employed to describe the convective motions and heat transfer in the liquid fuel region. Validation has been carried out with the experimental measurements of Miller and Ross [17] for flame spread over a 1-propanol narrow pool of different depths. The detailed 3-D predictions were analysed to reveal fine details of the underlying gas and liquid flow features; and shed further light on the resulting flame characteristics, which were challenging to obtain experimentally.

2. Numerical formulations

Flame spread over liquid fuels at subflash temperatures is a fully coupled problem between the gas and liquid phases via mass, momentum and energy exchanges at the fuel surface. A compressible solver for the gas phase and an incompressible solver for the liquid phase were formulated. Interface boundary conditions were given for the exchanges of mass, momentum and energy between the two phases. The

modelling approach was built on from our recent numerical study to investigate the effect of convective motion within the liquid fuel on the mass burning rate of pool fires [3], but with significant modifications to address the more complex underlying physics in the present problem and the treatment of fuel evaporation through the solution of the transport equations.

2.1 Gas phase solver

Flame spread at subflash temperatures is a transient combustion-induced buoyancy-driven compressible laminar flow. Previous study of Glassman and Dryer [8] indicated that radiative heat transfer can be neglected for alcohol fuels in their small-scale laboratory tests. Preliminary simulations were conducted using the same finite-volume-based radiation treatment in our recently published paper [3] to consider radiative heat transfer to the fuel surface. In line with the findings of Glassman and Dryer [8], no appreciable effects of radiative heat transfer on the predicted flame spread were found in the predictions. On such basis, radiative heat transfer was neglected in the present study.

The conservation equations for mass, species, momentum, and energy are given below:

$$\frac{\partial \rho}{\partial t} + \nabla \cdot (\rho \vec{U}) = 0 \quad (1)$$

$$\frac{\partial(\rho_m)}{\partial t} + \nabla \cdot (\rho_m \vec{U}) + \nabla \cdot (\rho_m \vec{V}_m) = \dot{\rho}_m^c \quad m = 1, \dots, N - 1 \quad (2)$$

$$\frac{\partial(\rho \vec{U})}{\partial t} + \nabla \cdot (\rho \vec{U} \vec{U}) = \nabla \cdot \bar{\tau} - \nabla p + \rho \vec{g} \quad (3)$$

$$\frac{\partial(\rho h_s)}{\partial t} + \nabla \cdot (\rho h_s \vec{U}) = \frac{\partial p}{\partial t} - \nabla \cdot \vec{q} + \dot{Q}^c \quad (4)$$

where t , ρ , \vec{U} , ρ_m , p , \vec{g} , h_s and N are time, density, velocity vector, species density, pressure, gravity, sensible enthalpy and number of species, respectively.

Species diffusion velocity is calculated by the mixture-averaged approach:

$$\vec{V}_m = -\frac{D_m}{X_m} \nabla X_m \quad (5)$$

where D_m and X_m are species mixture-averaged diffusion coefficient and molar fraction, respectively.

Viscous stress tensor is given by:

$$\bar{\tau} = -\frac{2}{3} \mu (\nabla \cdot \vec{U}) \bar{I} + \mu [\nabla \vec{U} + (\nabla \vec{U})^T] \quad (6)$$

where μ and \bar{I} are dynamic viscosity of the multi-component mixture and unit tensor, respectively.

Heat flux in the energy equation is determined by:

$$\vec{q} = -\lambda \nabla T + \rho \sum_{m=1}^N h_{s,m} Y_m \vec{V}_m \quad (7)$$

where λ , T and $h_{s,m}$ are the thermal conductivity of the mixture, temperature and species sensible enthalpy, respectively.

μ , λ and D_m are computed by the following semi-empirical formula [31]:

$$\mu = \sum_{m=1}^N \frac{X_m \mu_m}{\sum_{j=1}^N X_j \phi_{mj}} \quad (8)$$

$$\text{where } \phi_{mj} = \frac{1}{\sqrt{8}} \left(1 + \frac{W_m}{W_j}\right)^{-1/2} \left[1 + \left(\frac{\mu_m}{\mu_j}\right)^{1/2} \left(\frac{W_j}{W_m}\right)^{1/4}\right]^2 \quad (9)$$

$$\lambda = \frac{1}{2} \left(\sum_{m=1}^N X_m \lambda_m + \frac{1}{\sum_{m=1}^N X_m / \lambda_m} \right) \quad (10)$$

$$D_m = \frac{\sum_{j \neq m}^N (X_j + \varepsilon) W_j}{\bar{W} \sum_{j \neq m}^N (X_j + \varepsilon) D_{m,j}} \quad (11)$$

where W_j and \bar{W} are molar weight of species and mixture, respectively. μ_m and $D_{m,j}$ are calculated according to the standard kinetic theory [32], and λ_i is computed according to Warnatz [33].

A second-order one-step chemical reaction expression is used to determine the chemical source terms $\dot{\rho}_m^C$ and \dot{Q}^C . The global reaction can be written:



where ν_{O_2} , ν_{CO_2} and ν_{H_2O} are stoichiometric coefficients.

Chemical reaction rate is given by:

$$\dot{\omega}_r = A (\rho_F / W_F) (\rho_{O_2} / W_{O_2}) \exp(-E_a / RT) \quad (13)$$

where A is pre-exponential factor, ρ_F and ρ_{O_2} are species density of fuel vapor and oxygen, E_a activation energy, R universal gas constant. The chemical source terms are then calculated using the following equations:

$$\dot{\rho}_F^C = -W_F \dot{\omega}_r \quad (14)$$

$$\dot{\rho}_{O_2}^C = -\nu_{O_2} W_{O_2} \dot{\omega}_r \quad (15)$$

$$\dot{\rho}_{CO_2}^C = \nu_{CO_2} W_{CO_2} \dot{\omega}_r \quad (16)$$

$$\dot{\rho}_{H_2O}^C = \nu_{H_2O} W_{H_2O} \dot{\omega}_r \quad (17)$$

$$\dot{Q}^C = Q_r \dot{\omega}_r \quad (18)$$

where Q_r is the negative of the heat of reaction at absolute zero.

2.2 Liquid phase solver

The liquid fuel region is treated as a transient thermocapillary and buoyancy driven incompressible laminar flow. While the density of the liquid phase was assumed to be independent of pressure, temperature dependent thermophysical properties were used in the following transport equations:

$$\nabla \cdot \vec{U} = 0 \quad (19)$$

$$\frac{\partial(\rho\vec{U})}{\partial t} + \nabla \cdot (\rho\vec{U}\vec{U}) = \nabla \cdot \vec{\tau} - \nabla p + \rho\vec{g} \quad (20)$$

$$\frac{\partial(\rho h)}{\partial t} + \nabla \cdot (\rho h\vec{U}) = \nabla \cdot \left(\frac{k}{c_p} \nabla h \right) \quad (21)$$

where k and C_p are thermal conductivity and specific heat respectively. The pressure in Eq. (20) is defined as the relative pressure to the atmospheric pressure. The code uses the finite volume approach, the volume integral of the pressure gradient is converted into surface area integrals using the divergence theorem.

2.3 Interface conditions

The solutions of both the gas and liquid phases are closely coupled at the phase interface. Hence, the interface conditions of mass, momentum and energy need to be prescribed. These are described in the next few sub-sections.

2.3.1 Thermocapillary velocity

A Cartesian coordinate system is used. The fuel surface is in the X-Y plane. The thermocapillary-driven convective velocity at the fuel surface is related to the surface temperature gradient:

$$\mu_l \frac{\partial u_l}{\partial z} - \mu_g \frac{\partial u_g}{\partial z} = \frac{\partial \sigma}{\partial T} \frac{\partial T}{\partial x} \quad (22)$$

$$\mu_l \frac{\partial v_l}{\partial z} - \mu_g \frac{\partial v_g}{\partial z} = \frac{\partial \sigma}{\partial T} \frac{\partial T}{\partial y} \quad (23)$$

where the subscripts of l and g denote liquid phase and gas phase, respectively. $\frac{\partial \sigma}{\partial T}$ is the temperature coefficient of surface tension. The location of fuel surface is assumed to be fixed in the Z direction by neglecting surface recession resulting from evaporation.

2.3.2 Evaporation rate

As gas phase no-slip boundary condition is applied at the interface, the normal velocity component is zero. Therefore, the evaporation rate is determined by the vapor diffusive flux at the interface. The vapor molar concentration at the interface is

calculated according to the Clausius-Clapeyron relation, assuming an equilibrium condition and an ambient pressure of 1 atm:

$$X_{Equil} = \exp \left[\frac{\Delta H_v}{R_l} \left(\frac{1}{T_s} - \frac{1}{T_b} \right) \right] \quad (24)$$

where ΔH_v , R_l , T_s and T_b are heat of vaporization, fuel gas constant, surface temperature and boiling point, respectively. The evaporation rate is then given by:

$$\dot{m}'' = -\frac{\rho_F D_F}{X_F} \nabla X_F \quad (25)$$

2.3.3 Conjugate heat transfer

The gas phase flame feedback to the interface is used for heating and vaporization. At the interface, the following equations apply:

$$T_l = T_g \quad (26)$$

$$k \frac{\partial T_l}{\partial z} + \dot{m}'' \Delta H_v = \lambda \frac{\partial T_g}{\partial z} \quad (27)$$

3. Numerical methods

The numerical formulations described in the previous sections were implemented in the in-house version of the open-source computational fluid dynamics (CFD) toolbox OpenFOAM [34]. The code uses the efficient combination of the PISO and SIMPLE algorithms to handle the pressure-velocity coupling and update the solutions. The governing equations of each phase were discretized onto an orthogonal mesh using the control volume approach and solved separately in different computational regions. The solution procedure started with the liquid and then the gas phase to facilitate the use of the predicted interface conditions from the liquid phase as boundary conditions for the gas phase. The simulation was started by assuming an initial guess of the temperature distribution at the interface. The prescribed interface temperature was used to solve the corresponding energy transport equation to obtain a new temperature solution. This iterative process was repeated until the desired convergency criteria was satisfied.

The unsteady terms are discretized using a second-order backward differencing scheme. As the unsteady terms, convection terms and diffusion terms in the transport equations involve multi-physics and scales, they need to be treated with different numerical schemes. The convection terms behave differently for vectors and scalars. The convection term in the momentum equation is discretized using a second-order Gauss linear scheme to reduce numerical diffusion. The scalar convection terms are discretized using a second-order limited linear scheme to suppress any numerical oscillations. All the diffusion terms are discretized using a second-order Gauss linear scheme.

4. Problem descriptions

Model validation was conducted with the laboratory-scale tests of Miller and Ross [17] for pulsating and uniform spread over a narrow 1-propanol tray with different fuel depths. The length and width of the tray were 0.3 m and 0.02 m, respectively. The experiments covered fuel depths of 2 mm, 5 mm and 10 mm. The internal walls of the tray were insulated with glass to reduce heat losses to the walls.

4.1 Computational domain

Figure 1 illustrates the computational domain where the gas phase is shown in grey and liquid phase in red. To allow for the asymmetric flame propagation [6], the computational domain includes the whole tray width instead of using a symmetric boundary condition. The length of the liquid region is 0.16 m to reduce the computational cost, which is sufficient to capture characteristic spreading cycles. All the three tested fuel depths were simulated. Ignition was introduced near the left edge of the liquid region. To ensure that the left-side boundary of the gas region is less affected by the ignition-induced flow, the gas region was extended 0.03 m upstream of the fuel tray. The gas region was also laterally extended 0.01 m on both sides to better capture air entrainment from the surroundings. This choice was based on a preliminary simulation with a lateral extension of 0.02 m which did not show appreciable differences. The height of the gas region was 0.06 m to allow ample space above the flame.

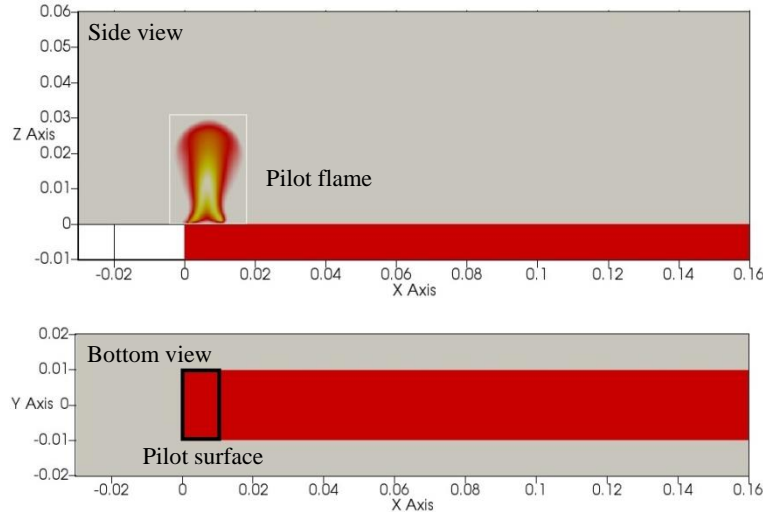


Fig. 1. Computational domain.

4.2 Properties for 1-propanol

The fuel is 1-propanol. Its thermo-physical properties are temperature-dependent. For instance, the viscosity can vary by more than 60% within the relevant temperature range. Four polynomials, represented by the following form, were fitted with the temperature-dependent properties listed in [37] for the density, thermal conductivity, specific heat capacity and viscosity.

$$P(T) = \beta_0 + \beta_1 T + \beta_2 T^2 + \beta_3 T^3 + \beta_4 T^4 + \beta_5 T^5 \quad (28)$$

The coefficients for the fitted properties are listed in Table 1 and the fitting curves are shown in Fig. 2. The heat of vaporization and boiling point appearing in Eq. (24) are 790 kJ/kg and 370.3 K [37], respectively. The temperature coefficient of surface tension in Eq. (22-23) is $-0.08 \text{ mN}/(\text{m} \cdot \text{K})$ [37].

Table 1 Thermo-physical properties for 1-propanol

Property	β_0	β_1	β_2	β_3	β_4	β_5
Density (kg/m^3)	-4.9672×10^3	93.0306	-0.5872	1.84×10^{-3}	-2.8755×10^{-6}	1.7949×10^{-9}
Specific heat ($\text{kJ}/\text{kg}/\text{K}$)	8.0983×10^3	-1312	0.8487	-274×10^{-3}	4.407×10^{-6}	-2.8301×10^{-9}
Viscosity ($\text{Pa} \cdot \text{s}$)	6.9389	-0.1067	6.5715×10^{-4}	-2.0256×10^{-6}	3.1217×10^{-9}	-1.9231×10^{-12}
Thermal conductivity ($\text{W}/\text{m}/\text{K}$)	7.1828	-0.1097	6.9108×10^{-4}	-2.1932×10^{-6}	3.4482×10^{-9}	-2.2436×10^{-12}

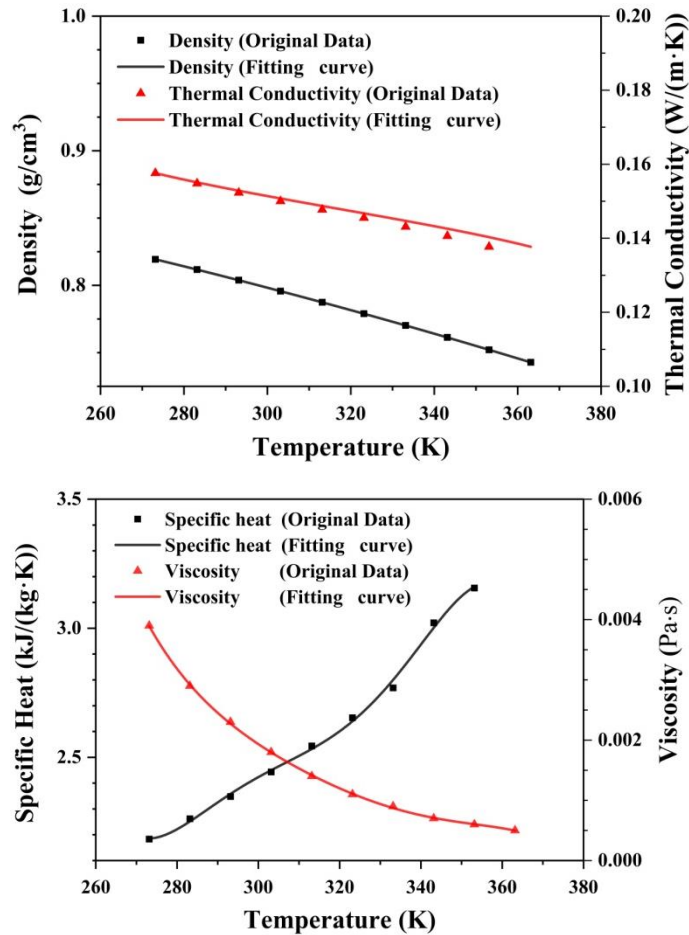


Fig. 2. Fitted thermo-physical properties for 1-propanol (The original property data was taken from [37]).

As the main body of the flame is mixing-controlled and non-premixed, the use of detailed chemistry is considered desirable but of relatively little benefit except for the small lean premixed flame during the flame jump stage. A detailed chemistry was

attempted in our preliminary study [3], which significantly increased the computational cost. Additional computational requirement also resulted from the associated need to compute species diffusion velocity by the mixture-averaged approach. However, no appreciable benefit was found. Hence, the following global reaction for 1-propanol is used [35]:



The activation energy in Eq. (13) is 30 kcal/gmol [35]. The pre-exponential factor is determined to be $2.55 \times 10^{11} \text{ m}^3/(\text{kmol} \cdot \text{s})$ by fitting to the measured laminar velocity under a test condition of 1 atm and 423 K, which was the only reported test condition in the experimental paper [36], as shown in Fig. 3.

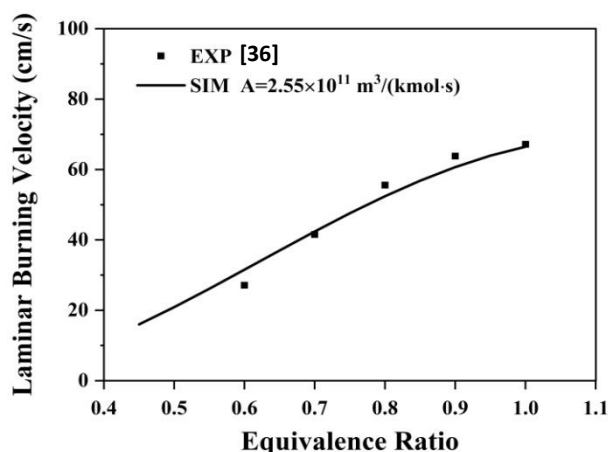


Fig. 3. Comparison of laminar burning velocity.

The flash temperature of 1-propanol is 298 K [17]. Two fuel temperatures were considered in the present study, i.e. 287.25 and 292.85 K, corresponding to the pulsating and uniform spread regimes [17].

4.3 The computational grids

Relatively fine grid resolution is required to capture the small-scale chemical and thermal processes in the present study, which involve complex flow and flame structures, sharp thermal gradient, vapor diffusion layer and recirculation cells at the interface. The height of the first cell next to the interface was set to 30 μm and 15 μm for the gas and liquid fuel regions, respectively. These were considered sufficient to resolve gradients at the interface according to Schiller et al. [22]. The grid height was increased gradually to 0.5 mm at $z = 3 \text{ mm}$ and then remained uniform in the gas region. The grid height in the liquid region was also gradually increased to 0.12 mm at the bottom plane. A uniform grid resolution was applied across the interface with grid size of 0.5 mm in both X and Y directions. The grid size in the gas region was gradually increased from the tray boundaries to the lateral domain boundaries. The main body of the gas region has a uniform grid size of 0.5 mm, resulting in approximately a total of 4 million cells for the case of 10 mm fuel depth.

Numerical simulations of such complex phenomena are sensitive to grid

resolutions. The above final choice of the grid resolutions was, hence, proceeded by a preliminary grid sensitivity study. While keeping the height of the first cell next to the interface in both the gas and liquid regions as described above, predictions were conducted with a uniform grid resolution of 0.25 mm (instead of 0.5 mm as described above) for the main body of the gas region. To reduce the computational cost the tray length was set to 0.1 m and the total cell number was approximately 8 million. The predicted flame thickness at the flame front, characterized by the maximum chemical reaction rate, was 4 mm for both grid resolutions, demonstrating that the reaction zones were well captured in both simulations. Figure 4 shows the results of the grid sensitivity study by comparing the predictions of the two sets of predictions for the location of the flame front and the length of the convective surface ahead of the flame front in the middle plane with each other and the measurements in [17]. The flame front was identified by the maximum chemical reaction rate immediately above the fuel surface while the convective flow front was artificially determined by the location where the flow velocity attenuated to 0.5 cm/s. For simulations with both resolutions, the predicted average spread rates and pulsating wavelengths agreed well with the measurements [17]. The two sets of predictions were very close prior to $t = 2$ s. A discrepancy appeared around $t = 2.25$ s, which was most likely due to insufficient resolution of the temperature gradient on the fuel surface, which governs the thermocapillary flow and has a distinct impact on the vaporization process and spread rate [6]. The predictions showed that the location of the flame front is nearly identical for the first four pulsating cycles, and the predicted thickness of the flame front is 4 mm for both grid sizes, demonstrating that a grid spacing of 0.5 mm is sufficient to resolve the reaction zone. Furthermore, for the considered flame spread, chemistry is not the limiting factor and chemical reaction rate does not significantly affect the spreading behavior. The predictions of flame spread are indeed sensitive to the grid resolution. Completely grid-independent results are difficult to achieve due to the coupled multi-physics and complexity of the thermocapillary driven flow [6]. To compromise between computational cost and grid-convergent results, a grid spacing of 0.5 mm was used for the horizontal resolution.

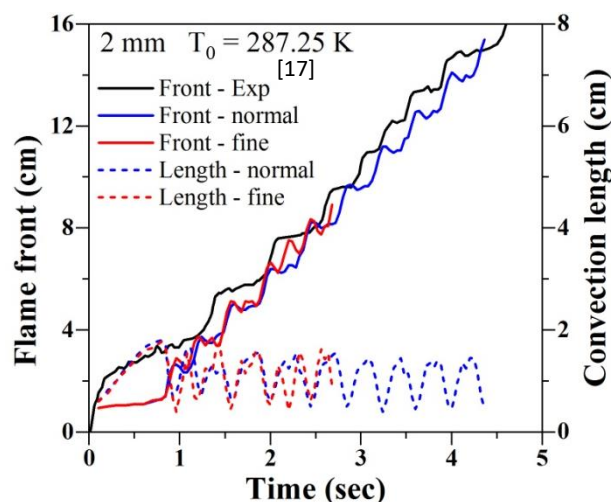


Fig. 4. Results of grid sensitivity study.

4.4 Ignition

At subflash temperatures, preheating is needed to create flammable mixture necessary for ignition. The ignition source above the fuel surface induces the surface convective flow which transports ignition energy away from the ignition site and increases the ignition time. In order to reduce the ignition time, a pilot flame with a prescribed vapor concentration as shown in Fig.1 was used in a similar way to that in the experiments of Li et al. [24]. The pilot surface was a rectangular region of a length of 1 cm on the left side of the fuel tray, where a constant vapor mass fraction of 0.3 was prescribed. The pilot flame had a dimension of $4\text{ mm} \times 4\text{ mm} \times 4\text{ mm}$, centrally 2 mm above the pilot surface. The temperature inside the ignition site was gradually increased to 1700 K over 1 ms, and the total ignition time was set to 20 ms. The ignition process was expected to affect the initial flame spread rate due to the ignition-induced surface flow. However, once the flame spread became self-sustaining, the spread rate was no longer affected by the pilot flame.

4.5 Initial and boundary conditions

Two initial fuel temperatures were considered, i.e. 287.3 K and 292.9 K, which correspond to flame spread in the pulsating and uniform regimes, respectively [17]. The initial temperature of the gas phase was 293 K for all the cases as it has little effect on the flame spread [11].

There exists a stratified vapor profile before the ignition due to evaporation. In our preliminary simulation, an initial constant vapor profile was initialized following Schiller et al. [22]. A trial simulation without initializing the vapor was also conducted for comparison. No appreciable difference was found between the two sets of predictions. Two major reasons can account for this. Firstly, the initial vapor concentration was low at subflash temperatures and the preheating from the flame was the dominant factor for the vapor distribution ahead of the flame front. Secondly, the predicted flame front started to propagate after a period of approximately 1 s as shown in Fig. 4. Within this period, a stratified vapor profile was established ahead of the flame front located approximately 1 mm away from the surface. Based on this finding, all the simulations were initialized with no presence of vapor in the gas phase.

As mentioned earlier, the flame anchors at the edges of the fuel tray. The thermal boundary condition on the tray walls would hence affect the flame spread, especially for the narrow trays considered in the present study. In the experiments of Ross and Miller [17], the tray walls were insulated. Adiabatic and no-slip boundary conditions were hence applied to all the solid walls, including the fuel container walls in the liquid phase and the ground floor at $Z=0$ plane in the gas phase. The lateral and top boundaries of the gas phase were set as a free boundary condition, which is a stable boundary condition for buoyancy-driven flows and incurs no spurious flows at the boundaries [3]. For the free boundary condition, a time-dependent convective equation is solved, allowing both inflow and outflow at the boundary.

4.6 Computational time step

The total computational cost is limited by the gas phase solver. In this study, both solvers run at an identical variable time step constrained by the gas phase CFL number, which was 0.2 for all the simulations. This time step was found to be sufficient to resolve the time scales in both liquid and gas phases in the present study.

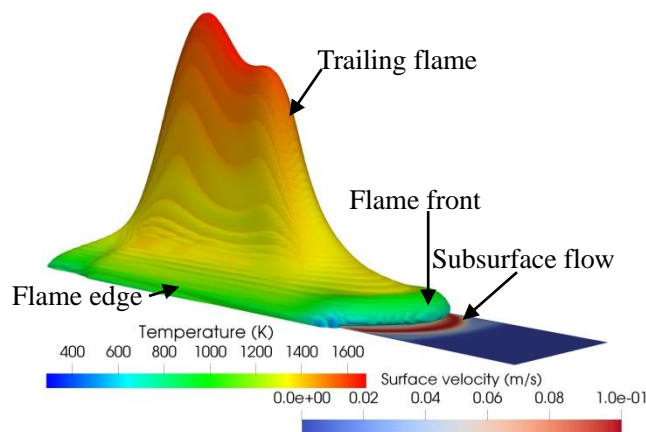


Fig. 5. Predicted flame shape over fuel surface with subsurface flow.

5. Results and discussion

The predicted flame spread over the fuel surface at $t=1.8$ s is shown in Fig. 5, represented by an iso-surface of chemical reaction rate coloured by temperature. The predicted trailing flame is anchored over the tray edges, which oscillates during spread. The spreading flame front resides over the fuel surface, preceded by a subsurface convective flow.

In the subsequent sections, results will be firstly presented for the validation, which will be followed by detailed discussion of the predictions for both uniform and pulsating spreads. All the length units in the figures are in meter, unless specifically designated.

5.1 Validation

The predicted flame fronts are compared with the experimental measurements in Fig. 6. The origins of the curves were shifted to the onset of the flame propagation following ignition. As the flame front was curved, its location was defined by that of the maximum chemical reaction rate in the $y=0$ plane. The predicted location of the flame front was in good agreement with the experimental data [17] for all the cases. Figure 6(a) on the left shows the predictions for fuel surface temperature of 287.25 K with the flame spread in the pulsating regime. The predicted pulsating wavelength, which is related to the convection length, i.e. the length between the flame front and the subsurface convective flow front, agrees well with the experimental measurements. The jump velocity, which is the spread rate during the jump stage, remains almost constant for all the cases at 13 cm/s. This is in excellent agreement with the

measured value of 12.5 cm/s. It is worth pointing out that the first pulsating cycle was significantly affected by the ignition. The convection length of the subsurface flow was also elongated due to the ignition delay, resulting in a long jump for the first cycle which gradually decreases over the next few cycles. Figure 6 (b) plots the predictions for the case of fuel temperature 292.85 K, which is 5.3 K below the flash temperature and in the uniform regime. The flame front propagates at uniform speed.

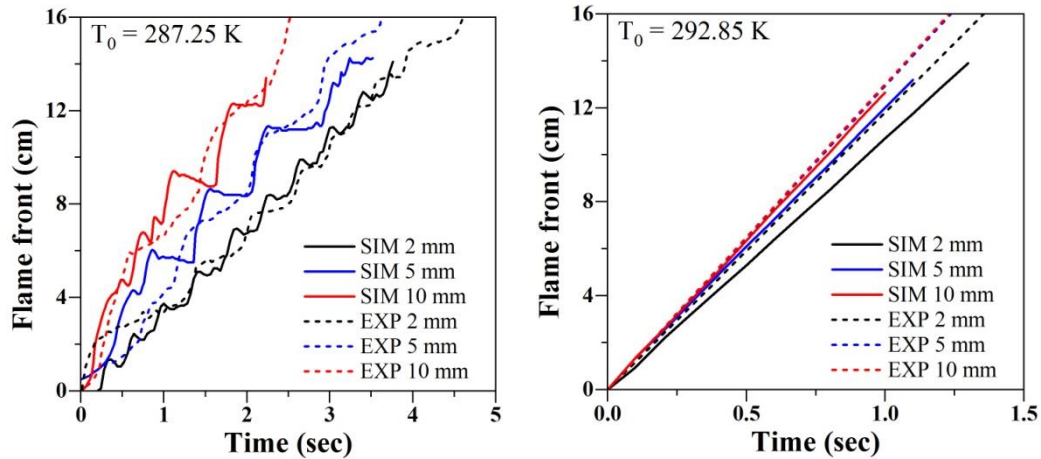


Fig. 6. Comparisons of flame front locations with the experiment data [17] (a) Pulsating spread; (b) uniform spread.

5.2 Uniform spread

When the fuel temperature is 292.85 K, the flame propagates at a constant rate as shown in Fig. 6. The distributions of the predicted field variables at the frontal inclined flame remain almost unchanged in relation to the flame front. Results of one instantaneous moment are analysed in Fig. 7, where the temperature distribution at the flame front in the middle plane was plotted. A lean flame front of a maximum temperature of about 1700K was predicted with an inclination angle of approximately 30 degrees. The flame front resides 0.8 mm above the fuel surface, characterized by the maximum chemical reaction rate. There exists a steep temperature gradient underneath the flame front, generating large heat feedback to the subsurface.

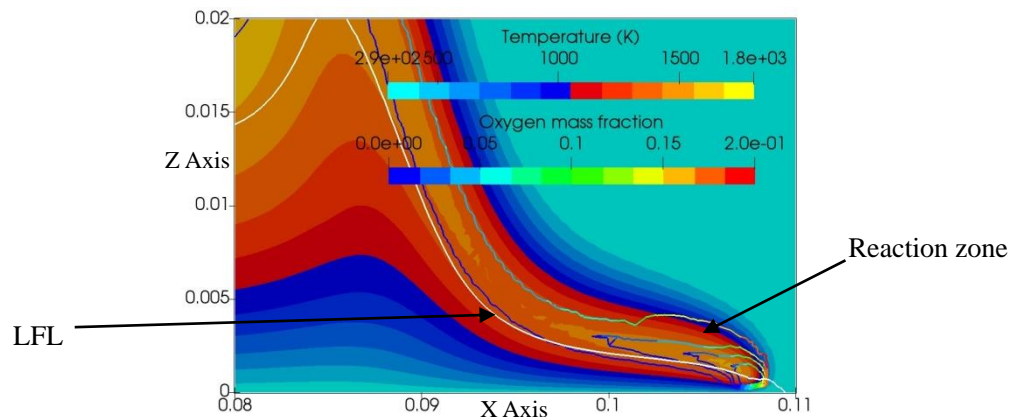


Fig. 7. Temperature distribution at the flame front on the middle plane for uniform spread over 2 mm deep pool. (The white line denotes LFL of 2.2% vapor molar fraction; the reaction zone is presented by contour lines of chemical reaction rates coloured by oxygen mass fraction.)

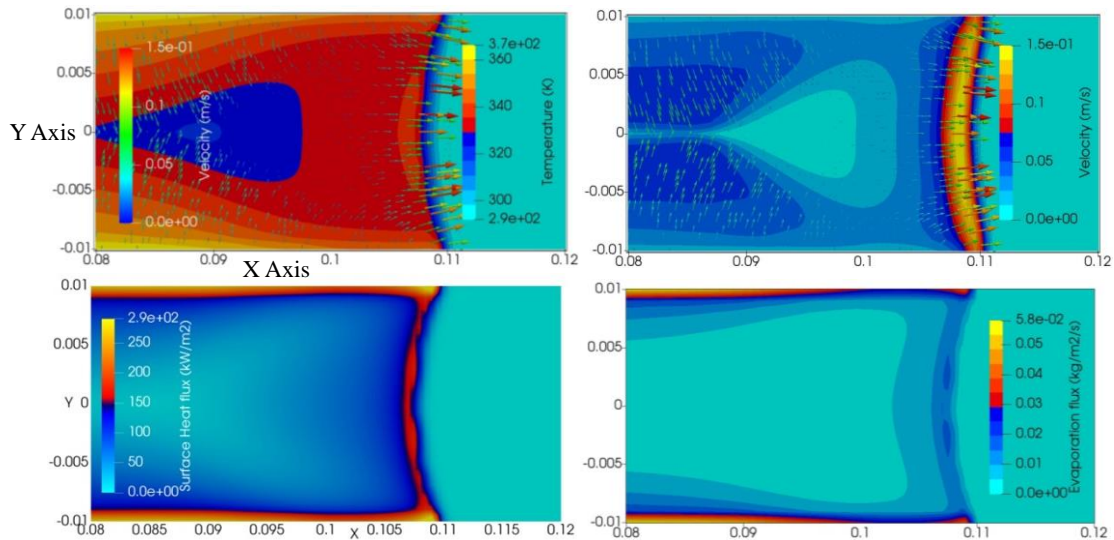


Fig. 8. Field parameters on the fuel surface for uniform spread over 2 mm deep pool.

The distributions of the predicted temperature, velocity, heat feedback on the fuel surface and evaporation mass flux around the flame front are shown on the fuel surface in Fig. 8. The predicted flame front is almost flat and slightly concave. The predicted surface temperature is higher at the tray edges and underneath the flame front, while it is relatively lower in the central region away from the flame edges. The temperature gradients induce both longitudinal and transverse surface flows. The transverse flows carry hot fluid at the tray edges towards the central region. There exists a narrow high-speed longitudinal flow resulting from the steep temperature gradient underneath the flame front. Ahead of the flame, little subsurface flow is observed. The maximum velocity of the surface flow is 15 cm/s, larger than the spread rate of 11 cm/s, which implies the existence of subsurface flow ahead of the flame front. The distributions of the heat feedback and evaporation mass flux follow the same pattern. The heat flux on the surface is high at the flame edges with a maximum value of 290 kW/m² as the flames are anchored there next to the adiabatic side wall. The heat flux behind the flame front is still relatively high at 160 kW/m² as the flame is attached to the fuel surface, leading to relatively high fuel evaporation rate to sustain the uniform spread. The evaporation mass flux has a maximum value of 0.058 kg/(m² · s) at the tray edges due to the high surface temperature and large vapor consumption rate. Underneath the flame front, the mass flux is around 0.02 kg/(m² · s). The mass flux is low in the central region since the gradients of both vapor concentration and temperature are small over this region.

Figure 9 shows the flow structures at the flame front in the middle plane for the case of uniform spread over 2 mm deep pool. The shaded colour contour is plotted with the mass fraction of the fuel vapor while the white line denotes LFL. The green curve is the isoline for oxygen mass fraction of 0.03. On the left of the curve, the oxygen mass fraction gradually decreases away from it while on its right, the oxygen mass fraction increases gradually. The inner red line encloses a small triangle region around the intersection of the white and green line. This is where the reaction rate

reached its maximum. The outer longer red curve represents the border beyond which the reaction rate decreases sharply. In other words, it encloses the reaction zone. The predicted velocity vectors were also superimposed over the shaded colour contour. Consistent with experimental observations of Ito et al. [9], a subsurface convective flow can be seen underneath the flame front; and the convective front is roughly 3mm ahead of the flame front, as estimated from Fig. 10 by treating the location of the maximum temperature as the flame front and the location of the convective front as the point when the velocity dropped to 1% of the maximum convective surface velocity. A boundary-type velocity profile is observed in the fuel region close to the fuel surface and its thickness is approximately 0.5 mm. A clockwise recirculation cell forms in the fuel region under the flame front induced by both the thermocapillary and viscous effects. This was also experimentally observed by Ito et al. [9]. The gas phase flow is dominated by an opposed buoyancy-driven flow at the flame front. The combination of the opposed buoyancy-driven flow and the concurrent subsurface flow induces an anti-clockwise recirculation cell that extends further backward underneath the flame front. This small recirculation cell plays an important role in the case of uniform spread since it facilitates the formation of a flammable mixture just ahead of the flame front. To the best of our knowledge, this is the first time that such recirculation cell is captured for the uniform spread regime. This was likely because its small size might be beyond the resolutions of previous experimental and numerical simulations.

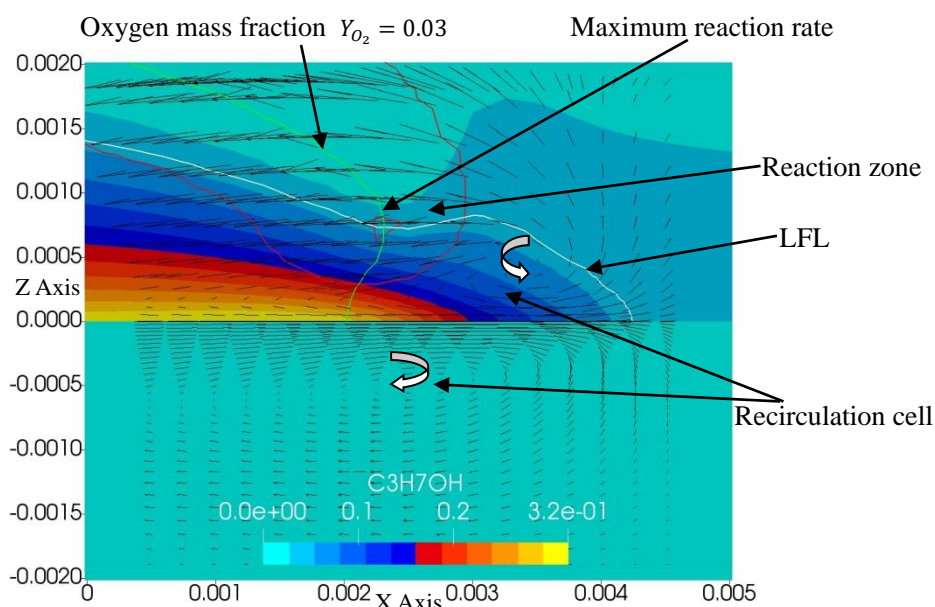


Fig. 9. Flow structures of the two phases at the flame front in the middle plane for the uniform spread over 2 mm deep pool.

The location of the flame front, defined by the maximum reaction rate as labelled in Fig. 9, coincides with the cross point of the LFL and the contour line of $Y_{O_2} = 0.03$. It is located about 0.8 mm above the fuel surface. There exists a small stratified premixed region within the LFL just ahead of the flame front. This premixed region is

vital to sustain the uniform spread. As mentioned above, there exists a subsurface flow ahead of the flame front, which preheats the fuel temperature above the flash point. As shown in Fig. 8, the evaporation rate just ahead of the flame front is high due to the preheating. Judging from the contour of vapour mass fraction in Fig. 9, the vapour is stratified with relatively large concentration gradients. Therefore, there exists significant vapour diffusive flux from both the preheated fuel surface and the diffusion region behind the flame front into the premixed region. The gas phase recirculation cell is also responsible for convecting fuel vapor into the premixed region and extending the premixed region upwards. It can be seen from Fig. 9 that the main body of the flame is of diffusion type while a small stratified premixed flame exists at the flame front sustaining the flame spreading. It should be clarified that for uniform flame spread, the spread rate is controlled by both the generation rate of flammable mixture ahead of the flame front and chemical reaction rate, and the generation rate is the limiting factor. Therefore, the spread rate is expected to be slightly smaller than the laminar flame speed. However, as the flammable mixture is stratified, it is difficult to make direct comparison between the flame tip propagation velocity and the laminar flame speed.

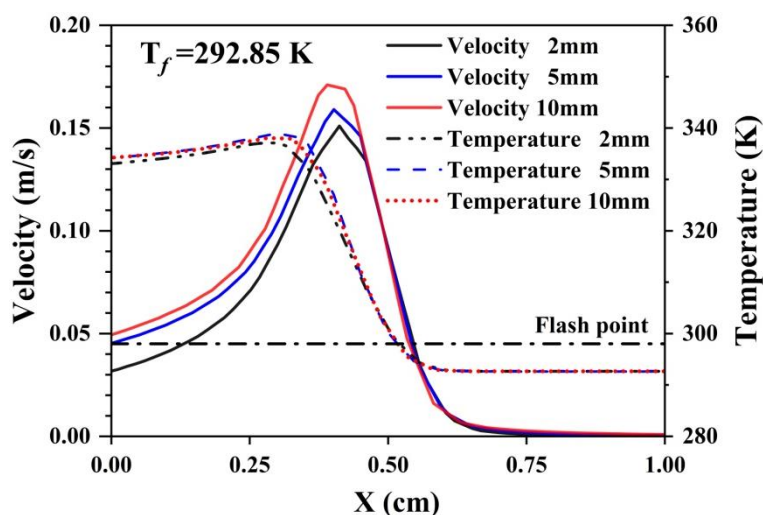


Fig. 10. Temperature and velocity profiles on the central line of the fuel surface for uniform spread with different pool depths.

Numerical simulations were subsequently conducted for uniform spread over fuel pools of different depths. The predicted flame spreads over trays of 5 mm and 10 mm deep behave similarly to that of 2 mm pool. The predicted profiles of the temperature and velocity on the central line of the fuel surface are compared in Fig. 10. The maximum surface temperature on the centreline is around 336 K and the surface temperature drops sharply to the initial temperature of 293.85 K within a distance of 2.5 mm. The distance between the maximum temperature and the flash point temperature (298.15 K for 1-propanol) is approximately 2 mm, over which the flammable mixture is generated. The maximum velocity is shifted ahead of the

maximum temperature approximately 1.25 mm since the surface flow is driven by the surface temperature gradient. The velocity also decays quickly to zero ahead of the flame front. There exists apparent subsurface flow behind the flame front, which transports vapor and energy towards the flame front.

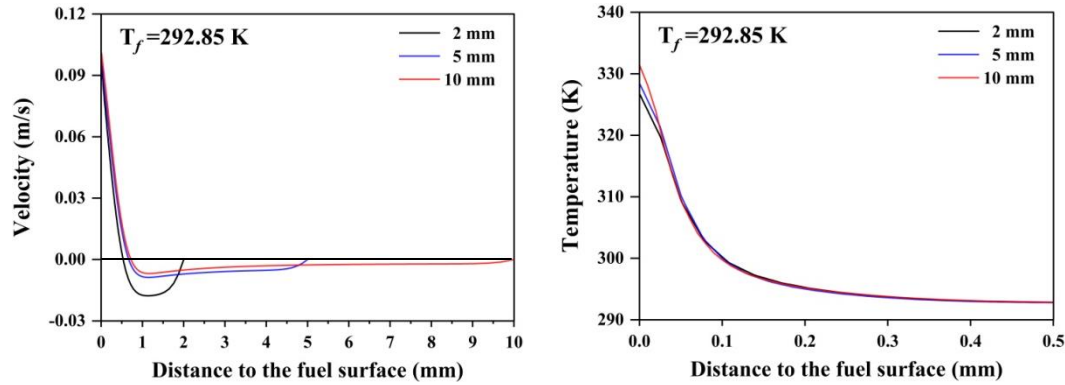


Fig. 11. Temperature and velocity profiles on the vertical line through the recirculation cell centre in the middle of the fuel region for uniform spread with different pool depths.

Although the maximum temperature only changes slightly with the fuel depth, an apparent difference can be seen for the maximum velocity. The maximum velocity is 15 cm/s, 16 cm/s and 17 cm/s for the cases of 2 mm, 5 mm and 10 mm deep pool, respectively. This difference lead to the increase of the flame spread rate with the increase of the fuel depth. To gain further insight of this difference, the profiles of temperature and velocity on the vertical line through the recirculation centre in the middle of the fuel region are examined for the cases of different fuel depths in Fig. 11. The straight horizontal line in Fig. 11 was intended to facilitate the identification of the thickness of the boundary-type surface flow.

It can be seen in Fig. 9 that the thickness of the boundary-type surface flow changes in the longitudinal direction. The location of the recirculation centre is a useful reference point for comparing the surface stress. The maximum velocities of the profiles are a little bit lower than the maximum velocities on the surface because the cell centre is behind the location of the maximum surface velocity. The recirculation flow extends fully into the tray bottom and the reverse flow tends to be weaker for the deeper tray due to mass continuity condition. The reverse flow affects the location of the recirculation centre, i.e. the thickness of the surface boundary flow. The recirculation centre shifts toward the bottom surface as the reverse flow weakens. The recirculation centre sits 5 mm, 7.5mm and 8 mm below the surface for the cases of 2 mm, 5 mm and 10 mm, respectively. Therefore, the surface stress decreases with an increase in fuel depth, resulting in the difference in the surface flow for different depths. Since the effect of fuel depth has dominant effect on the extent of the reverse flow, the momentum loss at the tray bottom is less relevant. Although fuel depth has a significant impact on the surface boundary flow, it has relatively little influence on the thermal boundary layer beneath the flame front for the uniform spread as seen in Fig. 11. This is because heat conduction is the controlling factor at this location. The

thermal boundary layer is very thin, roughly 0.3 mm at the recirculation centre.

Figure 12 shows the temperature distribution in a cross-section 5 cm behind the flame front. Due to the transverse temperature gradient mentioned above, a pair of counter-rotating vortices prevail in the cross-plane, which significantly enhances the heat transfer in the fuel region via convective motions. This flow condition prevails behind the flame front.

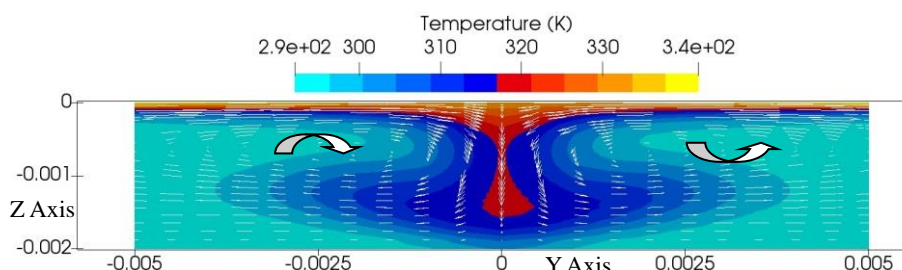


Fig. 12. Temperature contour and velocity vector in a cross-plane 5 cm behind the flame front during uniform spread.

5.3 Pulsating spread

For the cases of fuel temperature 287.25 K, the flame spread in the pulsating mode. It was shown in the previous section that an almost flat flame front was predicted for the uniform spread (Fig. 8), which is less affected by the tray edges. This is consistent with the numerical predictions of Cai et al. [28]. However, the tray edges have a significant influence on the flame front for the current narrow tray. Figure 13 presents the evolution of the flame front on the horizontal plane of $Z=1$ mm at four distinctive instantaneous moments for the case of 2 mm deep pool. The flame front was characterized by the contour lines of different chemical reaction rates as labelled in the figure. Alternate convex-concave flame fronts were predicted, consistent with the experimental observation for narrow trays of 1-2 cm width [6]. This phenomenon is thought to be caused by the opposite pulsating phases of the central part and the edges. The results suggested that four phases can be defined for the evolution of the flame front.

- In Phase 1, the jumping flame just stops, and the convection length drops to its minimum;
- Phase 2 corresponds to the moment when the flame front is in the crawling stage and the convection length is growing;
- Phase 3 is the moment when a flame jump, i.e. flame acceleration during the jump stage of the pulsating spread, is just about to occur and a maximum convection length is reached; and finally
- Phase 4 is an accelerating jumping stage with a rapidly decreasing convection length.

The contour of the vapor mass fraction is also presented in Fig. 13. The vapor concentration is high in the central region, demonstrating the existence of diffusive flux toward the flame. It can also be seen from Fig. 13 that the buoyancy-driven flow is directed inwards in an order of 20 cm/s, much larger than the flame spread rate and

that of the subsurface flow. Air entrainment flows are visible at the lateral boundaries, flowing toward the edge flames.

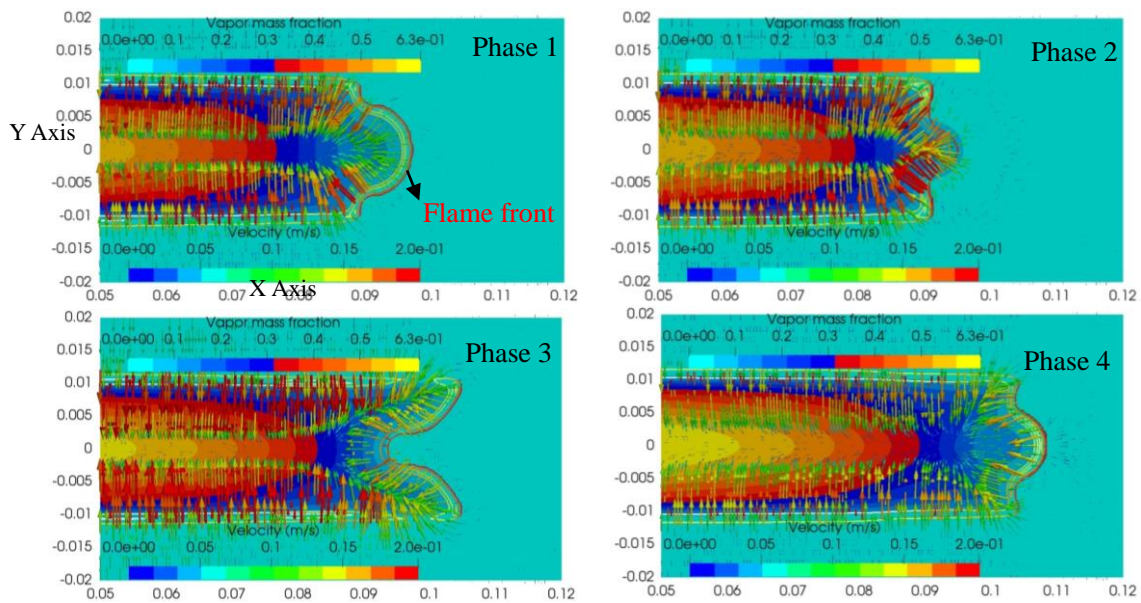


Fig. 13. Evolution of flame front on the horizontal plane of $z=1$ mm during the four phases of the pulsating spread over 2 mm deep pool.

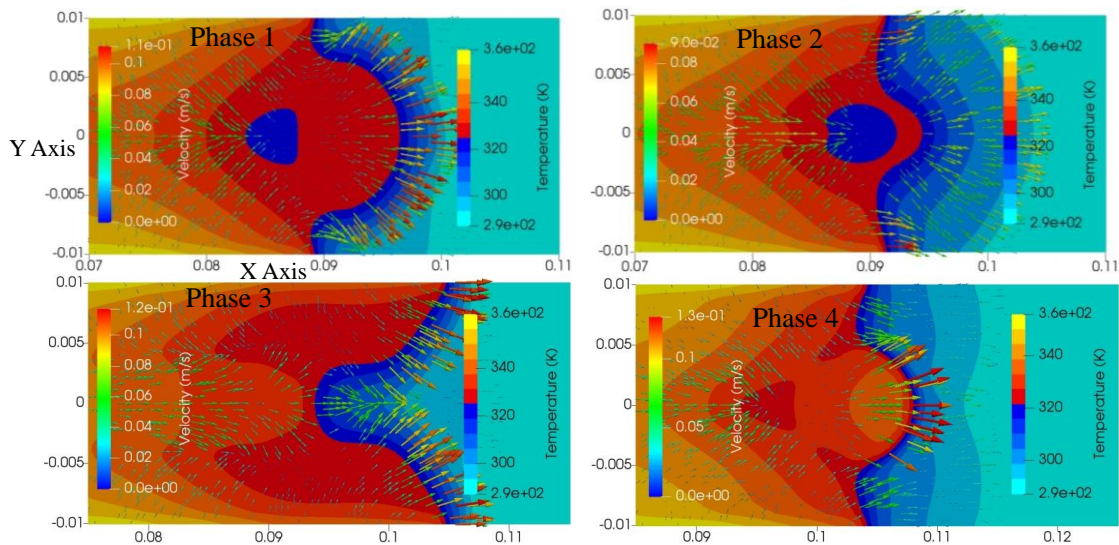


Fig. 14. Evolution of surface temperature on the fuel surface during the four phases of the pulsating spread over 2 mm deep pool.

The temperature distributions on the fuel surface during the four phases are examined in Fig. 14. The surface is heated by the flame heat feedback and the temperature distribution at the flame front exactly follows the profile of the flame fronts, which are represented by the red curves in the front. The predicted surface temperature is higher at the tray edges and behind the flame front, inducing both longitudinal and transverse flows towards the flame front. The preheated fuel surface is visible ahead of the flame front due to the subsurface flow for all the phases and the flame front always lags the subsurface flow front.

As the flame front jumps in a horizontal plane close the fuel surface, and the vertical velocity component can be neglected. The predicted velocity vectors on the interface are superimposed over the temperature contours in Fig. 14. During Phase 1, the velocity is high at the convex front, induced by the jump spread. The velocity decays quickly at the convex front and starts to accelerate near the edges caused by the acceleration of the edge flames during Phase 2. In Phase 3, the edge flames jump forward and extend towards the central regions while the central flame front retreats slightly and a concave flame front appears. Behind the concave flame, apparent flow motions towards the almost stagnant central flame exist. They transport hot fluid and facilitate the flame spread. During Phase 4, the edge flames are in a crawling stage and remain almost stagnant. On the contrary, the central flame starts to jump, gradually evolving into a convex shape.

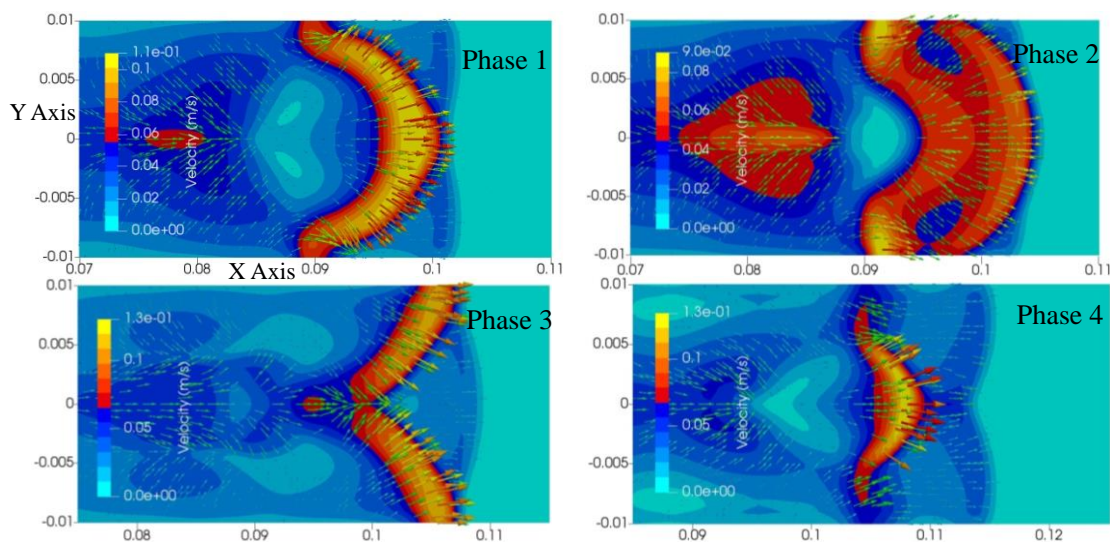


Fig. 15. Evolution of surface velocity on the fuel surface during the four phases of the pulsating spread over 2 mm deep pool.

As the flame resides on the fuel surface, the heat feedback is mainly through heat conduction. Figure 16 shows the surface heat flux during the four phases of the pulsating spread over 2 mm deep pool. The maximum surface heat flux occurs at the flame edges identical to the uniform spread. The heat flux at the flame front varies periodically during the pulsating cycle due to the flame front cyclically moving towards and away from the fuel surface. It is as low as 80 kW/m² at Phase 2 of the crawling stage and jumps to 160 kW/m² at Phase 4 of the jumping stage. The heat feedback is critical to the flame spread dynamics as it provides the heat source to fuel evaporation. It is also closely coupled with the dynamics of the flame spread via fuel evaporation and chemical reactions at the flame front.

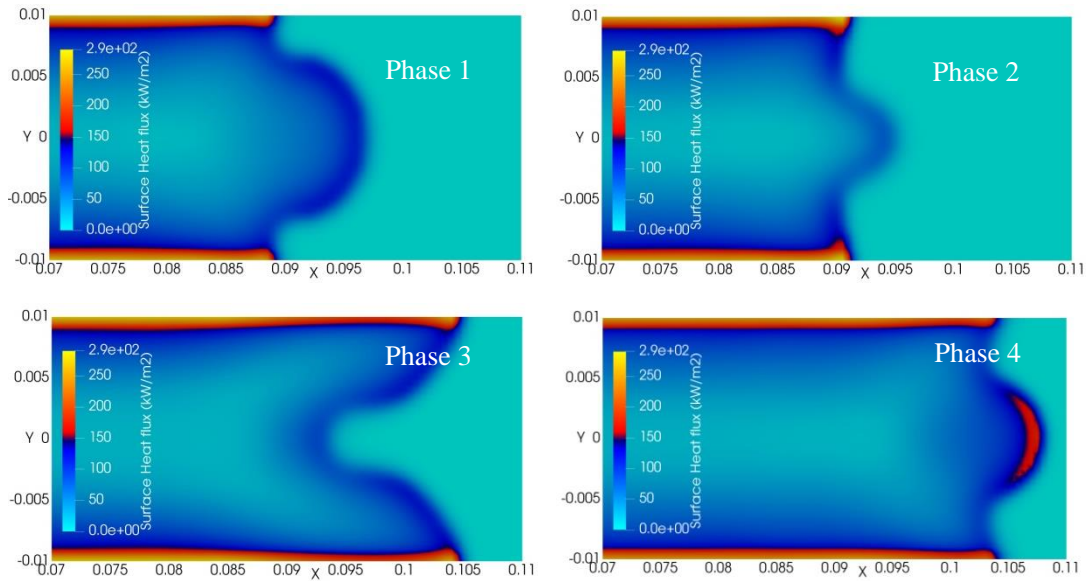


Fig. 16. Evolution of thermal feedback on the fuel surface during the four phases of the pulsating spread over 2 mm deep pool.

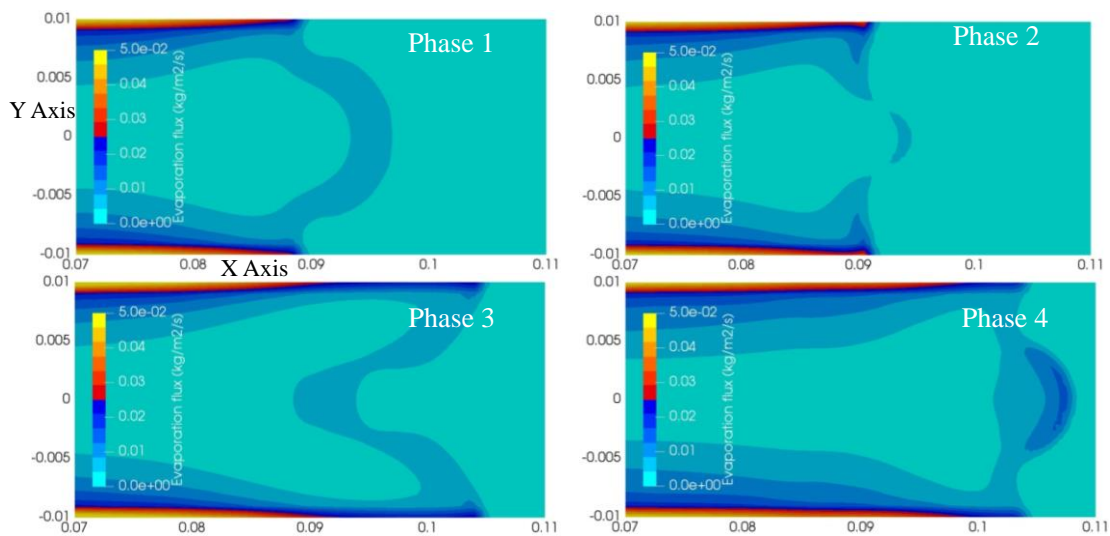


Fig. 17. Evolution of evaporation vapor flux on the fuel surface during the four phases of the pulsating spread over 2 mm deep pool.

Figure 15 shows the evolution of the fuel surface velocity during the four phases for the pulsating spread over 2 mm deep pool. A high-speed region exists ahead of the flame front and the subsurface flow front always precedes the flame front. The front of the subsurface flow is slightly disturbed by the pulsating flame so it also shows an oscillating convex-concave shape. After the jumping flame decelerates at Phase 1, the high-speed region propagates forwards, catching up with the subsurface flow front. Accordingly, the subsurface flow front accelerates and turns into a convex shape. Meanwhile, another high-speed region evolves at the flame front, driven by the thermocapillary effect as shown in Phase 2. The two high-speed regions induce two pairs of counter-rotating vortices in both the gas and liquid phases as shown later in Fig. 19. After the edge flames jump, the concave subsurface flow front appears as shown in Phase 4, and the spread cycle repeats.

The evolution of the evaporating vapor flux is shown in Fig. 17. The mass flux has a maximum value of $0.05 \text{ kg}/(\text{m}^2 \cdot \text{s})$ at the tray edges due to the high surface temperature and vapor consumption rate. Underneath the flame front, the mass flux is around $0.01 \text{ kg}/(\text{m}^2 \cdot \text{s})$ in Phase 1. The mass flux decreases underneath the flame front in Phase 2, and the flame front retreats from the surface. In Phase 4, a higher mass flux is seen because the flame front propagates towards the surface during the jumping stage, increasing the heat flux.

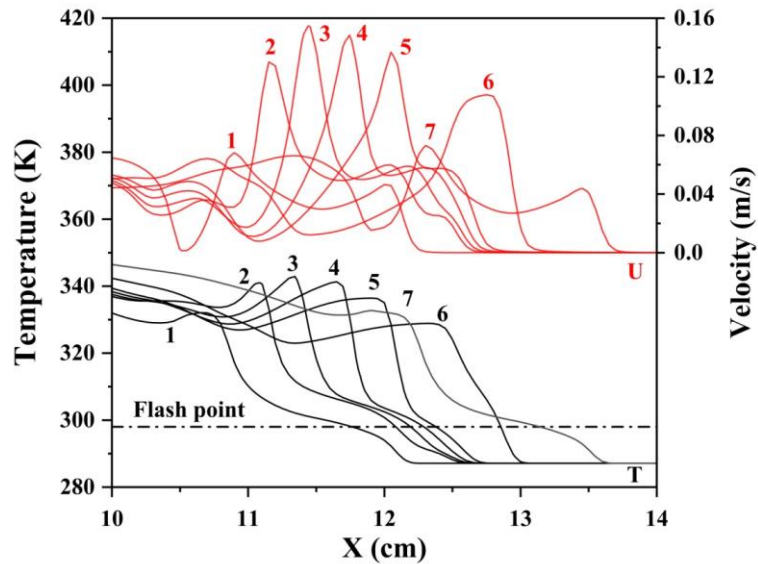


Fig. 18. Profiles of surface temperature and velocity on the central line at successive moments for the pulsating spread over 2 mm deep pool.

Profiles of surface temperature and velocity on the central line at successive moments are plotted in Fig. 18. The flame front is just about to accelerate at the instantaneous moment denoted by “1”, when the convection length between the flame front and the convection front reaches a maximum of 1.5 cm. The surface temperature drops sharply to a value above the flash point at the flame front and then steadily reduces to the initial temperature at the convection front. Fig. 18 also shows that the surface velocity peaks lag the corresponding temperature peaks as the velocities are induced by the temperature gradients. The surface temperature valley ahead of the flame front was not predicted in the current simulations. This is consistent with the numerical predictions of Schiller et al. [22]. The surface velocity at the instantaneous moment “1” does not drop monotonically ahead of the flame front, showing two peaks as previously explained. The instantaneous moments “2 to 5” correspond to the accelerating jump stage, during which both surface temperature and velocity are higher than that of “1”. The maximum surface velocity and temperature at the instantaneous moment “3” are 15 cm/s and 340 K, respectively, which are coincident with those of the uniform spread shown in Fig. 10. The flame front is almost stagnant at the instantaneous moment “6” with the maximum temperature dropping to 330K due to the flame front retreating from the surface. Both the temperature and velocity decrease linearly to the initial values. The flame front retreats at the instantaneous moment “7” with decreasing surface velocity and

increasing surface temperature as the flame front moves toward the surface and the flow motions behind the flame front carry hot fluid forwards as mentioned above. The elevated surface temperature facilitates the flame spread and the spread cycle repeats.

Figure 19 presents the evolution of flow structures at the flame front in the middle plane for the two phases of the pulsating spread over 2 mm deep pool. In Phase 1, the flame front stops behind the convection front due to insufficient flammable mixture ahead of the flame front to sustain the spread and a counter-rotating vortex pair forms at the flame front. The recirculation cell in the gas phase facilitates the built-up of flammable mixture by transporting high concentration vapor forwards. Subsequently in Phase 2, an opposed flow is induced by the buoyancy effect and the cessation of flame forward spread. However, the opposed flow deters the built-up of the flammable mixture and causes the flame front to retreat slightly. Accordingly, the flame inclination angle increases. As the convection front moves at almost constant rate, the convection length increases and the recirculation cells in both phases also extend forwards with a slightly decreasing height. The opposed flow gets stronger at phase 3, and the flame front slightly retreats. The opposed flow condition also further reduces the height of the gas phase recirculation cell and causes the flame inclination angle to decrease. Two counter-rotating vortex pairs, which were experimentally observed by Ito et al. [9], appear during Phase 3. One vortex pair is located just ahead of the flame front, induced by the thermocapillary effect while the other forms behind the convection front induced by the second peak velocity mentioned above. The second vortex pair is relatively weak in strength and die out quickly. As the flammable mixture reaches a critical height ahead of the flame front, a thermal runaway condition is achieved and the flame front jump again in Phase 4 and quickly catches up with the convection front. In the meantime, the flame inclination nearly diminishes, enhancing the heat flux onto the fuel surface. Subsequently, the flame front propagates downwards into the stratified vapor layer, increasing the chemical reaction rate to sustain the fast spread. The jump spread induces a concurrent flow condition ahead of the flame front due to thermal expansion and destroys the recirculation cell ahead of the flame front. This phenomenon was also captured by the numerical predictions of Schiller et al. [22]. The jump spread also induces two vortices, one below the flame front in the liquid phase and another beneath the inclined flame front in the gas phase. As the flame front catches up with the convection front, no adequate flammable mixture exists to sustain the fast spread, the spread stops as in Phase 1 and the spread cycle repeats. In addition, it can be seen from Fig. 19 that the flame structure of the pulsating spread is the same as that of the uniform spread.

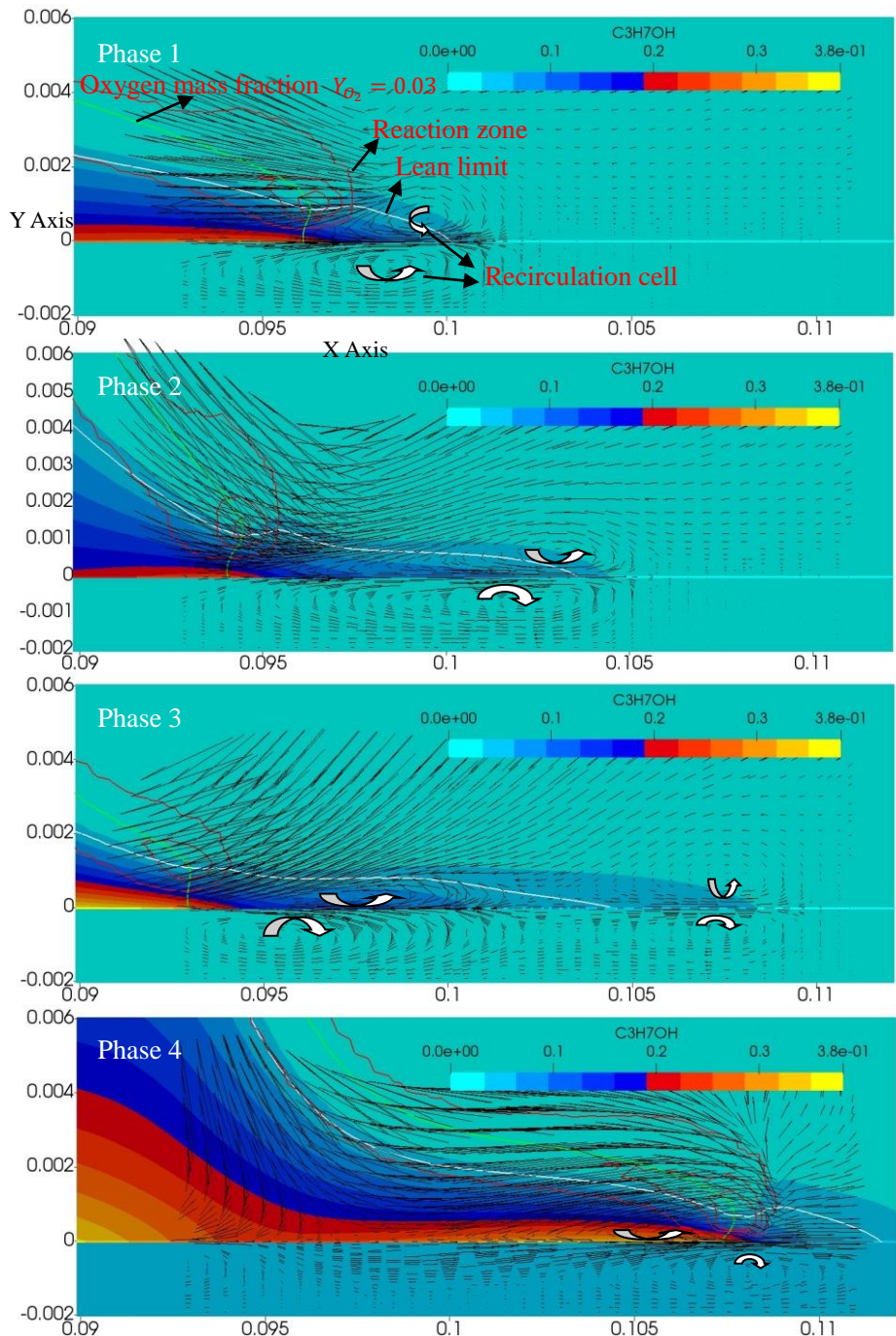


Fig. 19. Evolution of the flow structures in the first two phases at the flame front in the middle plane for the pulsating spread over the 2 mm deep pool.

Figure 20 shows the evolution of thermal boundary layer of the liquid phase underneath the flame front in the middle plane for the pulsating spread over the 2 mm deep pool. A wavy thermal boundary layer is observed underneath the flame front. The evolution of the thermal boundary layer is controlled by the convective motions, especially the clockwise recirculation cell, which transports hot fluid downwards, increasing the thickness of the thermal boundary layer. Meanwhile, it can also bring the cold fluid upwards, deterring its growth. Therefore, the wave-shaped thermal boundary layer forms as shown in Fig. 20, which is consistent with the experimental observation of Ito et al. [9]. During the crawling stage in Phase 2, the recirculation cell

ahead of the flame front results in a very thin thermal boundary layer. Its thickness is in the order of 0.3 mm. The location of the thin thermal boundary layer coincides with that of the surface temperature valley. However, the existence of the surface temperature valley is debatable as it was only observed in some tests and the mechanism for its formation is not clear. Konishi et al. [21] attributed the cause to the interaction of the subsurface flow and the buoyancy-induced liquid flow. However, it is generally accepted that the buoyancy effect of the liquid phase can be neglected in the pulsating flame spread [6]. As the thickness of the thermal boundary layer at the valley is only approximately 0.3 mm, there exists a steep temperature gradient near the surface, rendering measurements extremely difficult [6]. Although the surface temperature valley was predicted in the 2D simulation of Di Blasi et al. [26], the relatively coarse grid resolution used in their simulation casts doubt on the validity of the predictions for such fine details.

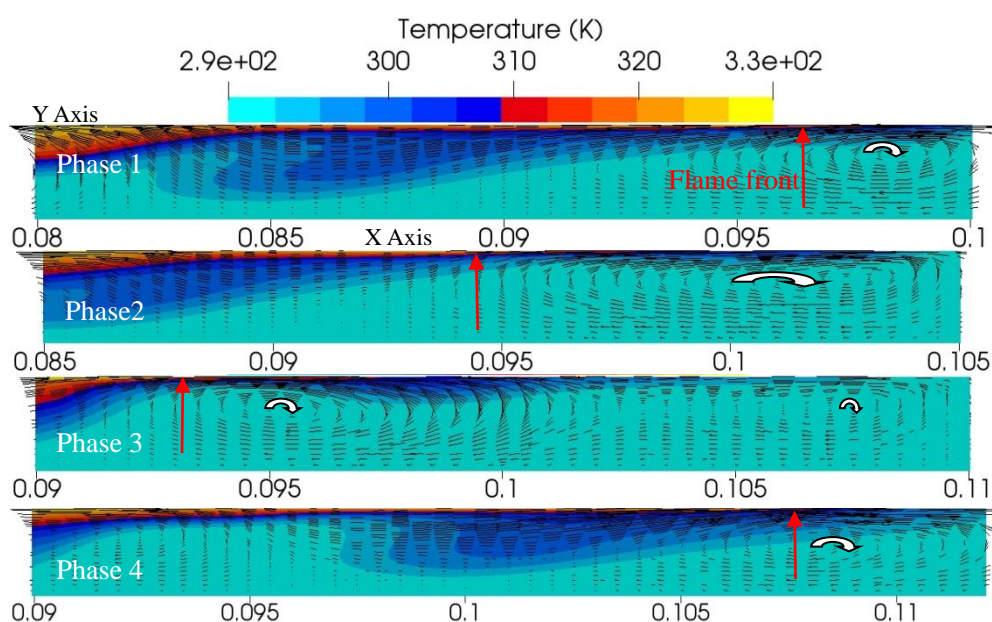


Fig. 20. Evolution of the thermal boundary layer of the liquid phases underneath the flame front in the middle plane for the pulsating spread over the 2 mm deep pool. (The location of the flame front is indicated by red arrows.)

The pulsating flame spread over the 5 mm and 10 mm deep pool behave similarly to that of the 2 mm deep pool, showing the same convex-concave flame front, flow, and thermal patterns. As previously explained for the uniform spread, the fuel depth affects the liquid surface stress, leading to different subsurface flow velocities. A fast subsurface flow results in a longer convection length, hence a longer pulsating wavelength as shown in Fig. 6. It is worth pointing out that the present predictions reveal slight flame retreats during the crawling stage for all the three pool depths as shown in Fig. 6. Although small flame retreats were also observed in the tests used for validation [17] for the case of 2 mm deep pool, contrary to our current predictions, no flame retreats were observed in the test [17] for both the 5 mm and 10 mm cases. The most possible reason for this discrepancy is due to the assumed adiabatic condition on the tray walls. As the flame anchors at the tray edges, it is sensitive to heat loss to the tray walls. Although the tray walls were insulated in the experiments, some heat

loss still existed. The adiabatic condition would result in higher temperature at the tray edges, inducing a stronger convex-concave flame front. Cai et al. [28] also predicted the flame retreats for the same geometry by assuming an adiabatic condition in their 3D simulation. However, no flame retreat was predicted by their 2D simulations using the same code [22]. Further investigation on the effect of the heat loss would be required to shed some light.

6. Concluding remarks

Fully coupled 3-D numerical formulations have been developed to explicitly solve the gas and liquid phase transport equations for flame spread over liquid fuels at subflash temperatures. The formulations were implemented within the frame of in-house version of the OpenFOAM code. A compressible solver was formulated for the flame propagation in the gas phase using a second-order one-step chemical reaction expression and mixture-averaged diffusion coefficients, while an incompressible solver with temperature-dependent thermo-physical properties was used to describe the convective motions and heat transfer in the liquid fuel region. Validation has been conducted with the measurements for both uniform and pulsating spreads over a narrow 1-propanol tray with different fuel depths [17]. The predicted jump velocity, flame front locations and pulsating wavelength, all achieved reasonably good agreement with the measurements. The results have provided numerical evidence that there always exists a subsurface convective flow ahead of the flame front for both the uniform and pulsating spreads due to the subsurface flow velocity being greater than the spread rate, further confirming thermocapillary-driven subsurface flow as the controlling mechanism for flame spread at subflash temperatures. The predictions illustrate in detail the structure of the spreading flame, which consists of a diffusion flame main body and a small stratified premixed flame at the front sustaining flame propagation as well as the alternating convex-concave flame fronts for the pulsating spread over a narrow fuel tray. The experimentally observed flame front retreat during pulsating spread was also captured and attributed to the buoyancy induced opposed flow, which deters the built-up of the flammable mixture ahead of the flame front. No obvious gas flow was predicted ahead of the flame front for uniform spread.

Additionally, the present study has revealed the following insight about the mechanisms and characteristics:

- Both longitudinal and transverse convective motions prevail at the fuel surface, transporting hot fluid towards the flame front and facilitating the flame spread. Although the transverse convective motion was postulated from the 2-D experimental measurements of Ross [6], it had not been captured by previous experiments or numerical simulations.
- At least one counter-rotating pair of recirculation cells always exists in both the gas and liquid phases. Their locations vary with flow conditions. In the uniform spread, the liquid phase recirculation cell is underneath the flame front, and the gas phase recirculation cell is just ahead of the flame front. During the crawling

stage of the pulsating spread, there initially exists one counter-rotating pair ahead of the flame front, subsequently two counter-rotating pairs appear before the flame jumps, one at the flame front and the other at the convection front. At the jumping stage of the pulsating spread, the counter-rotating pair is underneath the flame front. Only single liquid phase recirculation cell was captured in both previous experiments and numerical simulations for pulsating spread.

- The results have confirmed the existence of the gas phase recirculation cell at the flame front for the pulsating spread; and revealed for the first time their existence in the uniform spread regime. The gas phase recirculation cell plays an important role in the formation of the flammable mixture.
- The fuel depth has considerable effect on the surface stress of the liquid phase and the spread rate of the flame.
- For pulsating spread, the subsurface flow velocity does not always decay monotonically ahead of the flame front, showing two peaks before the flame jumps and inducing two counter-rotating pairs of recirculation cells.

Contrary to some previous experimental and 2-D numerical investigations, the results did not support the existence of the surface temperature valley. The predictions have illustrated a wavy thermal boundary layer underneath the flame front during the crawling stage in the pulsating spread. The location coincides with that of the predicted temperature valley in the previous 2-D simulation [26], indicating that the earlier identification of the temperature valley was likely caused by the lack of resolution to resolve the thin thermal boundary layer.

In summary, the present study demonstrates that the thermocapillary-driven subsurface flow is the controlling mechanism for both uniform and pulsating flame spread at subflash temperature. Ahead of the flame front, a stratified combustible mixture forms over the subsurface flow due to both evaporation and transportation of fuel vapour from behind the flame front by diffusive and convective mass fluxes. For a sufficiently high initial fuel temperature, the formation rate can be so fast that a uniform flame spread sustains. If the initial fuel temperature is low, the formation rate of the combustible mixture is insufficient to sustain a constant spread rate, the flame spread initially proceeds in a crawling spread and the flame jumps forwards as a critical flammable mixture forms, resulting in a pulsating flame spread.

References

- [1] K. Akita, Some problems of flame spread along a liquid surface, Symp. (Int.) Combust. 14 (1973) 1075-1083.
- [2] D. Villers, J.K. Platten, Coupled buoyancy and Marangoni convection in acetone: experiments and comparison with numerical simulations, J. Fluid Mech. 234 (1992) 487.
- [3] B.P. Xu, J. Wen, The effect of convective motion within liquid fuel on the mass burning rates of pool fires – A numerical study, Proc. Combust. Inst. 38 (2021)

4979-4986.

[4] R. Mackinven, J.G. Hansel, I. Glassman, Influence of laboratory parameters on flame spread across liquid fuels, *Combust. Sci. Technol.* 1 (1970) 293-306.

[5] W.A. Sirignano, A critical discussion of theories of flame spread across solid and liquid fuels, *Combust. Sci. Technol.* 6 (1972) 95-105.

[6] H.D. Ross, Ignition of and flame spread over laboratory-scale pools of pure liquid fuels, *Progress in Energy and Combustion Science* 20 (1994) 17-63.

[7] E. Degroote, P.L. Carcia-Ybarra, Flame spreading over liquid ethanol, *Eur. Phys. J. B* 13 (2000) 381-86.

[8] I. Glassman, F.L. Dryer, Flame spreading across liquid fuels, *Fire Safety Journal* 3 (1981) 123-138.

[9] A. Ito, D. Mastsuda, K. Saito, A study of flame spread over alcohols using holographic interferometry, *Combust. Flame* 83 (1991) 375-389.

[10] R. Mackinven, J.G. Hansel, I. Glassman, Influence of Laboratory Parameters on Flame Spread Across Liquid Fuels, *Combust. Sci. Technol.* 1 (1970) 293-306.

[11] T. Hirano, T. Suzuki, I. Mashiko, N. Tanabe, Gas movements in front of flames propagating across methanol, *Combust. Sci. Technol.* 22 (1980) 83-91.

[12] A. Ito, A. Narumi, T. Konishi, G. Tashtoush, K. Saito, C.J. Cremers, The measurement of transient two-dimensional profiles of velocity and fuel concentration over liquids, *J. Heat Transfer* 121 (1999) 413-419.

[13] K. Takahashi, Y. Kodaira, Y. Kudo, A. Ito, K. Saito, Effect of oxygen on flame spread over liquids, *Proc. Combust. Inst.* 31 (2007) 2625-2631.

[14] F.J. Miller, H.D. Ross, Smoke visualization of the gas-phase flow during flame spread across a liquid pool, *Proc. Combust. Inst.* 27 (1998) 2715-2722.

[15] H.D. Ross, F.J. Miller, Detailed experiments of flame spread across deep butanol pools, *Proc. Combust. Inst.* 26 (1996) 1327-1334.

[16] H.D. Ross, F.J. Miller, Flame spread across liquid pools with very low-speed opposed or concurrent airflow, *Proc. Combust. Inst.* 27 (1998) 2723-2729.

[17] H.D. Ross, F.J. Miller, Further observations of flame spread over laboratory-scale alcohol pools, *Symp. (Int.) Combust.* 24 (1992) 1703-1711.

[18] K.E. Torrance, R.L. Mahajan, Surface tension flows induced by a moving thermal source, *Combust. Sci. Technol.* 10 (1975) 125-136.

[19] T. Konishi, A. Ito, Y. Kudou, K. Saito, The role of a flame-induced liquid surface wave on pulsating flame spread, *Proc. Combust. Inst.* 29 (2002) 267-272.

[20] P.L. García-Ybarra, J.L. Castillo, J.C. Antoran, V. Sankovitch, J. San Martín, Study of the thermocapillary layer preceding slow, steadily spreading flames over

- liquid fuels, *Proc. Combust. Inst.* 26 (1996) 1469–1475.
- [21] T. Konishi, G. Tashtoush, A. Ito, A. Narumi, K. Saito, The effect of a cold temperature valley on pulsating flame spread over propanol, *Proc. Combust. Inst.* 28 (2000) 2819-2826.
- [22] D.N. Schiller, H.D. Ross, W.A. Sirignano, Computational analysis of flame spread across alcohol pools, *Combust. Sci. Technol.* 118 (1996) 205-258.
- [23] M.H. Li, Z.Z. Shu, L.F. Yi, B. Chen, Y.R. Zhao, S.W. Geng, Combustion behavior and oscillatory regime of flame spread over ethanol aqueous solution with different proportions, *Fuel* 253 (2019) 220-228.
- [24] M. Li, S. Lu, R. Chen, F. Guo, C. Wang, Experimental investigation on flame spread over diesel fuel near sea level and at high altitude, *Fuel* 184 (2016) 665-671.
- [25] M. Li, S. Lu, R. Chen, C. Wang, Pulsating behaviors of flame spread across n-butanol fuel surface, *Appl. Therm. Eng.* 112 (2016) 1445-1451.
- [26] C. Di Blasi, S. Crescitelli, G. Russo, Model of pulsating flame spread across liquid fuels, *Symp. (Int.) Combust.* 23 (1991) 1669-1675.
- [27] J.S. Cai, F. Liu, A. William, Three-dimensional structures of flames over liquid trays, *Combust. Sci. Technol.* 175 (2003) 2113–2139.
- [28] J.S. Cai, F. Liu, A. William, Three-dimensional flame propagation above liquid trays, *Combust. Sci. Technol.* 174 (2002) 5–34.
- [29] I. Kim, W.A. Sirignano, Computational study of opposed-force-flow flame spread across propanol pools, *Combust. Flame* 132 (2003) 611–27.
- [30] F.J. Miller, H.D. Ross, I. Kim, W.A. Sirignano, Parametric investigations of pulsating flame spread across 1-butanol pools, *Combust. Flame* 28 (2000) 2827-2834.
- [31] R.B. Bird, W.E. Stewart, E.N. Lightfoot, *Transport Phenomena*, John Wiley and Sons, New York, 1960.
- [32] J.O. Hirschfelder, C.F. Curtiss, R.B. Bird, *Molecular Theory of Gases and Liquids*, John Wiley and Sons, New York, 1954.
- [33] J. Warnatz, Influence of transport models and boundary conditions on flame structure, *Numerical Methods in Flame Propagation*, Wiesbaden, 1982.
- [34] H.G. Weller, G. Tabor, A.D. Gosman, C. Fureby, Application of a flame-wrinkling les combustion model to a turbulent mixing layer, *Symp. (Int.) Combust.* 27 (1998) 899-907.
- [35] C.K. Westbrook, F.L. Dryer, Simplified Reaction Mechanisms for the Oxidation of Hydrocarbon Fuels in Flames, *Combust. Sci. Technol.* 27 (1981) 31-43,
- [36] W. Li, Y. Zhang, B. Mei, Y. Li, C. Cao, J. Zou, J. yang, Z. Cheng, Experimental

and kinetic modeling study of n-propanol and i-propanol combustion: Flow reactor pyrolysis and laminar flame propagation, *Combust. Flame* 207 (2019) 171-185.

[37] BASF, n-Propanol, Technical Information Data Sheet, TI/E-CPI 1018e, August 2020.